

Downloaded from https://academic.oup.com/mnras/article/502/3/3664/6128658 by guest on 28 January 2023

# Dispersion measure distributions of fast radio bursts due to the intergalactic medium

Isabel Medlock<sup>★</sup> and Renyue Cen<sup>★</sup>

Department of Astrophysical Sciences, Princeton University, Princeton, NJ 08544, USA

Accepted 2021 January 25. Received 2020 December 30; in original form 2020 August 31

#### **ABSTRACT**

Utilizing cosmological hydrodynamic simulations, we quantify the distributions of the dispersion measure (DM) of fast radio bursts (FRBs). We examine the contributions of cold, warm-hot, and hot gas to the total DM. We find that the hot gas component  $(T > 10^7 \text{K})$ , on average, makes a minor contribution ( $\leq 5$  per cent) to the overall DM. Cold  $(T < 10^5 \text{K})$  and warm-hot  $(T = 10^5 - 10^7 \text{K})$  gas components make comparable contributions to DM for FRBs at z = 1, with the former component making an increasingly larger contribution towards higher redshift. We provide a detailed DM distribution of FRBs at z = 0.25 to z = 2 that may be compared to observations. We also compute the relation between the Compton y parameter and DM, finding a strong correlation,  $y \propto DM^4$ , providing an additional, independent constraint on the nature of the DM of FRBs.

Key words: intergalactic medium - fast radio bursts - methods: numerical - software: simulations.

#### 1 INTRODUCTION

The thermodynamic evolution of the intergalactic medium (IGM) is now substantially understood with the aid of *ab initio* cosmological hydrodynamic simulations. The most robust prediction from these simulations is that 40-50 per cent of all baryons in the present universe are in the warm-hot intergalactic medium (WHIM) of temperature  $10^5-10^7$  K and over density 10-300 (e.g. Cen & Ostriker 1999; Davé et al. 2001). These baryons can account for the long-standing missing baryon problem (Persic & Salucci 1992; Fukugita, Hogan & Peebles 1998), in which the sum of all other well-measured baryonic components (stars, X-ray emitting gas, Ly $\alpha$  forest, molecular, and atomic gas in galaxies, etc) falls significantly short of the baryonic density inferred from the cosmic microwave background observations and the big bang nucleosynthesis (e.g. Kirkman et al. 2003; Komatsu et al. 2009).

For at least the low temperature ( $T \le 10^6$  K) portion, the WHIM has been convincingly confirmed by a number of observations in the farultraviolet portion of QSO spectra from HST and the Far Ultraviolet Spectroscopic Explorer (FUSE), through the O VI λλ1032, 1038 absorption lines that peak at  $T \sim 3 \times 10^5$  K when collisionally ionized (e.g. Oegerle et al. 2000; Tripp & Savage 2000; Tripp, Savage & Jenkins 2000; Savage et al. 2002; Prochaska et al. 2004; Sembach et al. 2004; Danforth & Shull 2005; Danforth et al. 2006; Cooksey et al. 2008; Danforth & Shull 2008; Thom & Chen 2008a, b; Tripp et al. 2008) and Ne VIII  $\lambda\lambda770$ , 780 absorption lines that peak at  $T\sim$  $7 \times 10^5$ K in collisional ionization equilibrium (Savage et al. 2005; Narayanan, Wakker & Savage 2009; Narayanan et al. 2011; Tripp et al. 2011) as well as by the broad Ly $\alpha$  absorption lines (Danforth, Stocke & Shull 2010; Savage, Lehner & Narayanan 2011b; Savage et al. 2011a). Confirmation of the hotter portion of the WHIM is less certain (e.g. Nicastro et al. 2018). Measurements of the Sunyaev-Zel'dovich effect from filaments of the cosmic web, where most

\* E-mail: imedlock@princeton.edu (IM); cen@astro.princeton.edu (RC)

of the WHIM resides, are also consistent with predictions (e.g. de Graaff et al. 2017; Tanimura et al. 2018).

One tool that can aid the search for the 'missing' baryons is the dispersion measure (DM) of extragalactic emitters, in particular, radio sources. As the DM is only a function of the electron density distribution, it can serve to quantify and locate baryons within the IGM. One promising source is the relatively recently discovered fast radio bursts (FRB). FRBs are millisecond-long extragalactic pulses of radio waves with fluxes of 50 mJy to 100 Jy (Petroff, Hessels & Lorimer 2019). The first FRB is reported by Lorimer et al. (2007), discovered in a search of the Pulsar Survey of the Magellanic Clouds (Lorimer et al. (2007). Four more cases are reported by Thornton et al. (2013), confirming the discovery of a new phenomenon and coining the term 'fast radio burst'. Since the initial discovery, over 100 bursts have been detected and verified (Petroff et al. 2016).

The use of DM measurements from extragalactic sources has been examined previously with probes of gamma-ray bursts, assuming a homogeneous universe (Ioka 2003; Inoue 2004). More recently, McQuinn (2013) performed a pioneering study to compute, analytically, the mean and standard deviation of the DM, considering an inhomogeneous universe. Extending this work, we examine the distribution of the DMs of FRBs, as a function of redshift, utilizing cosmological hydrodynamic simulations of the intergalactic medium. We quantify separate contributions of various phases of gas, allowing us to better understand the contribution of the IGM. Moreover, we examine the relationship between the DM and the thermal Sunyaev–Zel'dovich effect (the Compton y parameter) that may be verified observationally in the future and provides a new way to probe the WHIM.

## 2 COSMOLOGICAL SIMULATIONS AND METHODS

#### 2.1 Cosmological simulations

The data used to calculate DM distributions comes from cosmological hydrodynamic simulations of the evolution of the IGM with

**Table 1.** The key parameters for the simulations including box and cell size.

Constant	Value
h	0.7
$\Omega_{matter}$	0.28
$\Omega_{\Lambda}$	0.72
$\Omega_{baryon}$	0.046
Box size L	$50~{ m Mpc}{ m h}^{-1}$
Number of cells dark matter particle mass in a cell	$\begin{array}{c} 2048 \\ 1.1 \times 10^7 \; M_{\odot} \end{array}$
Mean baryonic mass in a cell	$2.6\times10^5~M_{\odot}$

a WMAP5-normalized standard cold dark matter model (Cen & Chisari 2011), with cosmological parameters listed in Table 1. The initial conditions are produced using the COSMICS software package which uses multiscale Gaussian random fields (Bertschinger 2001).

The simulation advances on a uniform grid. Star formation, supernova feedback, and all radiative processes are taken into account. The simulation matches relatively well with observational data, suggesting that it is an accurate model of the universe (Cen & Chisari 2011). Each simulation output is composed of a grid of 2048<sup>3</sup> cells, with each cell containing values for total gas density, temperature, velocity, H I density, He I density, He II density, electron density, and others.

#### 2.2 DM and the Sunyaev-Zel'dovich effect

The observed total DM of FRBs is the sum of three components,

$$DM_{obs} = DM_{MW} + DM_{IGM} + \frac{DM_{Host}}{1 + \tau},$$
(1)

where  $\mathrm{DM_{MW}}$  is the contribution to the total DM of the Milky Way which depends on the galactic latitude of the source b, among other factors,  $\mathrm{DM_{IGM}}$  is the contribution of the IGM,  $\mathrm{DM_{Host}}$  is the contribution of the host, and z is the redshift of the source (Petroff et al. 2019). In this paper, we will focus solely on the contribution of the IGM to the DM. However, for  $\mathrm{DM_{Host}}$  and  $\mathrm{DM_{MW}}$ , there has been a number of studies devoted to them (e.g. Keating & Pen 2020; Niino 2020).

The dispersion measure is defined as

$$DM = \int_0^d \frac{n_e(l)}{1+z} dl. \tag{2}$$

where d is the distance to the source,  $n_e$  is the electron density, z is the redshift, and l is the comoving path-length. Of the FRBs observed so far, the range of DMs has been from 109.61 to 2596.1 pc cm<sup>-3</sup> (Petroff et al. 2019).

The mean DM due to a uniform ionized IGM is (Deng & Zhang 2014)

$$\langle \mathrm{DM}_{\mathrm{IGM}} \rangle = A \int_0^z \frac{(1+z)x(z)dz}{\sqrt{\Omega_{\mathrm{m}}(1+z)^3 + \Omega_{\Lambda}}},\tag{3}$$

where A is a constant equal to 933 pc cm<sup>-3</sup> (for the standard *Planck* cosmological parameters used), x(z) is the ionization fraction function dependent of redshift,  $\Omega_{\rm m}$ , is the energy density of matter, and  $\Omega_{\Lambda}$  is the cosmological constant.

Additionally, we investigate how the Compton y parameter correlates with the DM, for just WHIM as well as for all gas,

$$y = \int_0^d \frac{kT\sigma_{\rm T}}{m_{\rm e}c^2} \cdot n_{\rm e}dl,\tag{4}$$

where y is the dimensionless Compton y parameter, k is Boltzmann's constant, T is temperature,  $\sigma_T$  is the Thomson cross-section of the electron,  $m_e$  is mass of electron, c is speed of light, and  $n_e$  is electron density. The Compton y parameter quantifies the mean change (increase) in the energy of a photon as it scatters with hot electrons in the intervening space between the source and the observer.

#### 2.3 Numerical integrations for DM and y

Using the simulation data, we calculate the distribution of the DM for an FRB up to z=2. In addition to calculating the total DM, we calculate the individual contributions of the cold, warm-hot (or WHIM), and hot temperature regimes. Cold is defined as any cell with a temperature less than  $10^5$  K, warm-hot as any cell with a temperature between  $10^5$  and  $10^7$  K, and hot as any cell with a temperature greater than  $10^7$  K.

To calculate the DM, we integrate the density over the distance for which FRBs are usually found (z=1) using equation (2). To calculate free electron density  $n_e$  for each cell we read in the density values for the total density, density of Hydrogen-I, density of Helium-Ia, and density of Helium-II. Using the equation

$$n_{\rm e} = (1+z)^3 (n_{\rm HII} + 0.25 n_{\rm HeII} + 0.5 n_{\rm HeIII}),$$
 (5)

where  $n_{\rm H\,II}$ ,  $n_{\rm He\,II}$ , and  $n_{\rm He\,III}$  are comoving number density of H II, He II, and He III. We then multiply  $n_{\rm e}$  by the cell size. Note that the simulations solve the rate equations for the primordial gas. Thus, all species, H I, H II, He I, He II, and He III, are followed in the simulations. Of course H I and He I do not contribute to  $n_{\rm e}$ .

We repeat this procedure on a randomly selected column. We integrate by adding up all the individual electron densities from each cell in the selected column and multiplying by the column depth.

In order to integrate over the distance to FRBs, it is necessary to stack the cubes of data covering the redshift range of the light cone in question. For example, each cube of data has a comoving side length of 71.43 Mpc but the comoving distance from z = 0to z = 1 is 3343.7 Mpc, meaning that we need to stack a total of 46.8 cube's lengths. For each of these cubes, a random light cone or column is selected to integrate over. The simulation data has outputs at a handful of redshifts, z = 0, 0.25, 0.5, 0.75, 1.0, etc. For each FRB redshift, we optimally choose the number of simulation boxes at these discrete redshifts to stack through the light cone. In order to calculate the number of boxes needed for each redshift, we calculate the comoving distance to each redshift. We start using the data for a particular redshift at a distance halfway between that redshift and the previous one. For example, z = 0.25 is calculated to begin 1011.8 Mpc away. So for the first half of that distance, the first 505.72 Mpc, we use simulation data for z = 0 and for the remaining half of the distance we use simulation data for z = 0.25. These calculations are repeated for the remaining redshifts. So in the end, we determine that we have to stack a total distance of 505.72 Mpc for z = 0 output, for z = 0.25 output a total distance of 950.73 Mpc, and so on as shown in Fig. 1.

With each new cube that we stack, we select a new random column to integrate over. To account for partial boxes we round up and iterate through that number of boxes. We then multiply the total column density by the ratio of boxes needed to cover the appropriate distance (which could include a partial box) to the number actually included

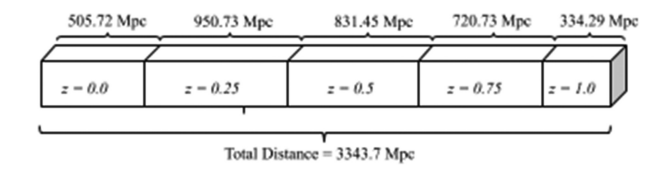


**Figure 1.** To integrate to an appropriate distance we stack the cubes of the simulation data. For the first half of the distance to a particular redshift, we use the previous redshift and for the second half use the redshift we were stacking towards, as shown. In the end, we needed 7.08 boxes for redshift 0, 13.31 boxes for redshift 0.25, 11.64 boxes for redshift 0.5, 10.09 boxes for redshift 0.75, and 4.68 boxes for redshift 1.

in the calculation (which must be a whole number). For example, for redshift 0, to achieve a distance of 505.72 Mpc, we need 7.08 boxes, so we add columns for eight boxes and then multiply that result by 7.08/8.

We repeat the procedure outlined above for 10000 trials and then examine the resulting distribution of the DMs, also looking at the distributions of the contributions of different temperatures towards the total DM.

In addition to looking at the contribution of different temperature regimes to the DM, we examine the contribution to the DM of solely the IGM versus that of all gas. The procedure is the same as that for calculating the total DM but excluding any cells in the integration that had density greater than 100 times the mean gas density at the redshift. We note the choice of overdensity of 100 is consistent with the convention of the definition of the virial radius, within which the overdensity is 200, which for an isothermal density profile would translate to a density of 100 at the virial radius, A small variation in this overdensity threshold, such as adopting the definition of Bryan & Norman (1998), does not materially alter the results of the IGM contribution to the DM distribution.

A similar procedure is used to numerically compute y parameter.

#### 3 RESULTS

#### 3.1 Detailed DM distributions

Fig. 2 shows the distribution of the total DM to z = 1, as well as the contribution of various phases of gas. In Table 2, we numerate the mean and dispersion of the total DM and each of the three separate gas components. We see that the total DM is  $919 \pm 202.3$  pc cm<sup>-3</sup>, and in agreement with the results of McQuinn (2013), who obtains a value of approximately 1000 pc cm<sup>-3</sup>. The standard deviation of 202 pc cm<sup>-3</sup> also agrees with 100-400 pc cm<sup>-3</sup> estimated by McQuinn (2013) for an FRB at z = 0.5 - 1. In addition to the distribution of the total DM, we also calculate the distribution for each of the three phases of gas according to the temperature, allowing for a better understanding of the contribution of various phases of gas. McQuinn (2013) also calculates the contribution from gas lower than 106 K, for which we can not make direct comparison due to a mismatch in temperature ranges. For comparison, the observed DMs of 100 FRBs are shown as green 'x' in Fig. 2, with no dependence on the y-axis. The estimated redshifts of these FRBs range from 0.05 to 2.10 (Petroff et al. 2016).

Table 2 shows the mean and standard deviation for the total DM as well as the DM for each temperature regime for FRBs up to z=2. At all redshifts, the cold and warm-hot gas make up the vast majority of the contribution to DM. At z=1 these two components have similar contributions, 432 pc cm<sup>-3</sup> for cold gas and 456 pc cm<sup>-3</sup> for warm-hot gas, respectively. The warm-hot gas makes an increasingly more dominant contribution to the total DM at z<1, while the cold

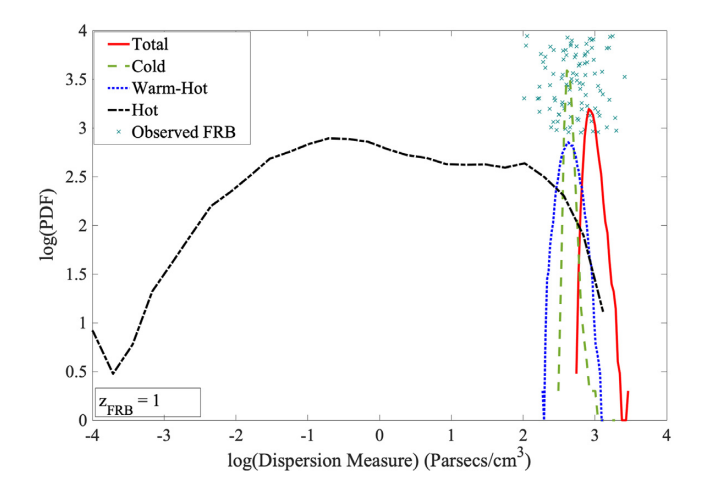


**Figure 2.** Shows the distribution of calculated DMs, both total and by temperature regime. A total of  $10\,000$  DM for  $10\,000$  (light cone) sightlines are used. The *y*-axis represents the number of light cones per DM bin. The solid red curve represents the total DM, including all temperature regimes. The cold DM (green dashed curve) is calculated for gas with temperatures less than  $10^5$  K. The warm-hot DM (blue dotted curve) is calculated for gas with temperatures  $10^5-10^7$  K. The hot DM (black dot—dashed curve) is calculated for gas with temperature greater than  $10^7$  K. The teal x's represent the DMs of 100 observed FRBs, without reference to the *y*-axis (Petroff et al. 2016).

component does at z > 1. Overall, the cold gas component displays the least variation with a standard deviation of 75.6 pc cm<sup>-3</sup>, while the hot component shows the most variation with a standard deviation of  $132.4 \text{ pc cm}^{-3}$ . These findings can be well explained as follows. The cold gas is mostly in the form of Ly $\alpha$  forest, residing in moderate density regions with relatively small density contrast (e.g. Davé et al. 1999; Danforth et al. 2006), hence, a relatively small dispersion of DM. Most of the warm-hot gas occurs at redshift below about z = 1. While the cold gas component is increasingly more important at z = 1 and becomes dominant beyond z = 2, the warm-hot gas makes up a somewhat larger fraction 40 - 50 per cent as compared to about 30 - 35 per cent for the cold component at z = 0. As noted in Cen & Ostriker (1999), the gravitational shock heating due to development and collapse of large-scale structure in the universe, to form groups and clusters of galaxies along with filaments and pancakes, beginning at around z = 3, to be able to heat the IGM to temperatures above 10<sup>5</sup> K. The mass fraction of WHIM becomes comparable to that of cold component by  $z \sim 1$ . The cold component that is heated by photoionization decreases with decreasing redshift when an increasing fraction of it is heated up by shock heating, but it remains the dominant component until  $z \sim 2$ . The mass fraction of WHIM becomes comparable to that of cold component by  $z \sim 1$ .

The hot temperature often has close to zero contribution but shows much more deviation, sometimes contributing on the order of  $200-600 \text{ pc cm}^{-3}$ . Fig. 2 does not show the full range of DMs for the hot temperature regime, as it is cut off at  $\log(\text{DM}) = 10^{-4}$ . However, roughly half of the trials result in a hot DM contribution less than that. The hot gas mostly resides in rich groups and clusters of galaxies and subtends a relatively small cross-section and a large mean free path, hence, the relatively large dispersion.

In order to better understand the breakdown of contributions of each temperature regime, we additionally plot in Fig. 3 the fractional contribution for both the case when we include all gas (both inside and outside the virial radius; left-hand panel) and when including gas in the IGM only (outside the virial radius). We calculate fractional

95.29

96.39

97.0

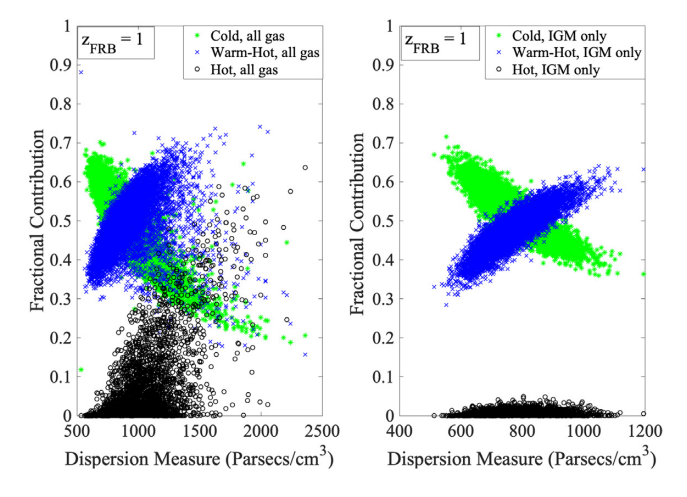
Mean (pc cm $^{-3}$ )  $SD (pc cm^{-3})$ 0.5 1.5 2.0 0.5 1.5 2.0 1.0 1.0 7. 202.33 207.67 Total 441.83 919.08 1384.3 1831.4 138.18 231.94 Cold 196.4 432.88 789.55 1136.1 26.34 75.63 72.62 102.74 Warm-hot 226.44 456.31 565.17 664.01 92.08 132.43 147.64 160.85

30.88

82.32

29.57

**Table 2.** The mean and standard deviation of the DM for the total gas and the three gas phases for FRBs at z = 0.5, z = 1, z = 1.5, and z = 2.



29.89

18.99

Hot

**Figure 3.** Plot of the fractional contribution of the cold, warm-hot, and hot temperature regimes to the DM of an object at redshift 1 as a function of total DM. Fractional contribution is defined by dividing the contribution to the DM of a single phase of gas over then entire DM. (a) Shows the results when considering all gas, including galaxies. (b) Shows the results when considering only the IGM, which is the low density gas.

distribution by dividing the DM from cells within temperatures for the desired gas phase by the total calculated DM.

As can be seen, when including all gas, the DM contributions from the warm-hot and hot gas components display significant scattering. As total DM increases, so does the fractional contribution of the warm-hot gas, just as that of the cold regime decreases. The contribution of the hot regime is often low, but there are many exceptions. The hot gas showed the most variation in fractional contribution as would be expected from Table 2. When including only the DM due to the IGM, the trends are significantly tighter, with the scatters largely suppressed, leaving behind only three well-defined islands. The contributions from the hot temperature regime are all less than 10 per cent, so we can infer that when considering all gas, most of the contribution from the hot regime comes from inside dark matter haloes. The fact that there are significant differences for the warm-hot gas contribution, with and without warm-hot gas inside the virial radius, indicates that WHIM gas inside the virial radius make a significant but not dominant contribution. For example, at DM = 1500 pc cm<sup>-3</sup>, the fractional contribution of warm-hot gas reaches about 70 per cent when warm-hot gas inside the virial radius is also included (left-hand panel), as compared to 63 per cent when warmhot gas inside the virial radius is excluded, causing about a 10 per cent difference. To clarify, we note that this difference is real in the sense that the possible variations due to stacking has been properly taken into account, where for the many light cones constructed, a single column in the simulation box (even across different redshifts) is seldom drawn twice.

Given the increasing FRB sample with increasing redshift, we calculate the DM distribution for FRBs at several redshifts, beyond

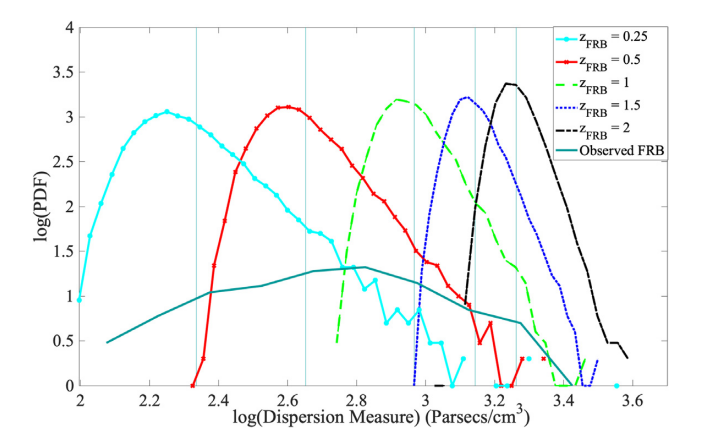


**Figure 4.** Log-log plot of the probability distribution function of the total DM in pc cm<sup>-3</sup> for FRBs at redshifts 0.25, 0.5, 1, 1.5, and 2. The results are from 10 000 trials. The predicted mean contribution to DM from the IGM based on (3) for each redshift are plotted as horizontal lines. Again, we include a distribution of observed FRB data.

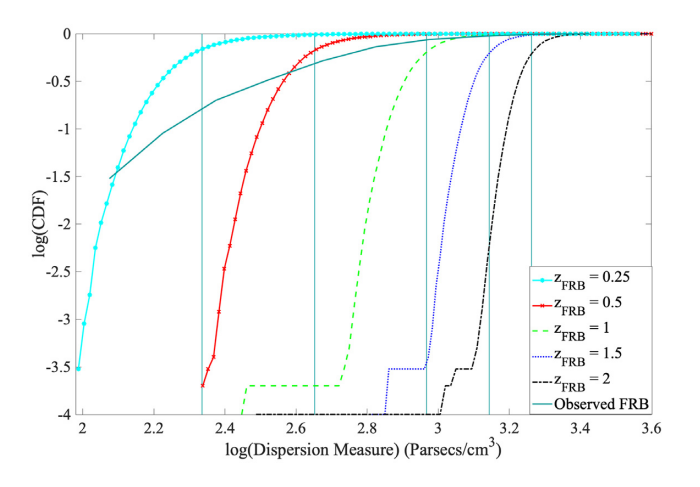


**Figure 5.** Log-log plot of the cumulative distribution function of the total DM in pc cm<sup>-3</sup> for FRBs at redshifts 0.25, 0.5, 1, 1.5, and 2. The results are from 10 000 trials. The predicted mean contribution to DM from the IGM based on (3) for each redshift are plotted as horizontal lines. Again, we include a distribution of observed FRB data.

the range z=0.5-1, first calculated by McQuinn (2013). We plot the probability density function (PDF) of the DM in Fig. 4 and the cumulative density function (CDF) of the DM in Fig. 5 for FRBs at five different redshifts: 0.25, 0.5, 1, 1.5, and 2. Since the DM distribution at a given redshift is not exactly Gaussian, we tabulate the median and percentiles for each distribution in Table 3. The median value of the DM at redshift 1 is 2.13 times the value of that at redshift 0.5, while the median value at redshift 2 is 2.04 times the value at redshift 1. The table will be useful for comparing with observations.

**Table 3.** Median and 5 per cent, 25 per cent, 75 per cent, and 95 per cent percentile values of the calculated DMs, in units of pc cm $^{-3}$ .

Redshift	5 per cent	25 per cent	Median	75 per cent	95 per cent
$z_{FRB} = 0.25$	130.7	160.8	190.4	235.1	366.7
$z_{FRB} = 0.5$	301.4	358.8	413.0	487.3	683.8
$z_{FRB} = 1.0$	692.8	793.4	882.1	1000.9	1261.5
$z_{\text{FRB}} = 1.5$	1128.3	1250.0	1349.8	1484.0	1764.6
$z_{FRB} = 2.0$	1530.0	1675.4	1796.5	1950.3	2260.2

Also shown in Figs 4 and 5 is the distribution of the DMs of 100 observed FRB, with the range of redshifts from z = 0.05-2.20. The mean DM of the 100 observed FRBs is 660.1843 pc cm<sup>-3</sup> with a standard deviation of 463.1225 pc cm<sup>-3</sup>. The peak of this distribution falls around 630 pc cm<sup>-3</sup>, which is within the DM distributions of redshift 0.5 and 1. Based on this observed distribution of DM of these 100 FRBs, we infer that the mean inferred redshift of the observational data is 0.5039 with a standard deviation of 0.4327 (Petroff et al. 2016), in agreement with observations.

The  $DM_{IGM}$  from a uniform ionized IGM, according to equation (3), are shown as vertical lines for the five redshifts distributions computed, to compare theory to our results. We find that the lines do, in fact, fall near the mean of each of the distributions, offering an additional validation of our results.

Finally, we note that the results presented here, for both the mean DM and its dispersion, are unlikely affected significantly by numerical resolutions of the simulation. This is because all the gas components in the IGM are adequately resolved. At the mean density, the Jeans length at z = 1 (as an example) for photoionized gas is about 2.5 comoving Mpc, more than an order of magnitude larger than our resolution of 35 comoving kpc. The two hotter components are also adequately resolved. For example, the Jeans length for  $10^5$  K at an overdensity of 100 is 0.82 comoving Mpc at z = 1.

### 3.2 Correlations between DM and y

We now turn to the correlation between the Compton y parameter and DM, considering, in two separate cases, gas of all temperatures and solely the warm-hot gas. The results are displayed as scatter plots in Fig. 6, in the left-hand and right-hand panel, respectively.

We see a clear correlation between the *y* parameter and the DM. We fit the data according to a linear model in the log-log plot. For all gas our best fit is found to be

$$\log(y) = 4.0883 \log(DM) - 18.673,\tag{6}$$

where DM is in units of pc cm<sup>-3</sup>. In terms of goodness of fit, this model has  $R^2$  value of 0.73. The 95 per cent confidence bounds for the first coefficients are 4.04 and 4.137. For the second coefficient, they are -18.82 and -18.53.

For the case with only warm-hot gas, the best fit is

$$\log(y) = 2.1952 \log(DM) - 12.483. \tag{7}$$

Here, the 95 per cent confidence bounds for the first coefficients are 2.17 and 2.22. For the second coefficient, the confidence bounds are -12.55 and -12.42. The  $R^2$  value is 0.77.

Comparing the fits, we observe that the fit for total gas has a steeper slope, which is expected as the Compton y parameter tends to increase more quickly in the case of all gas than just warm-hot gas. The mean Compton y parameter for the case of all gas is  $4.2 \times 10^{-7}$  with a standard deviation of  $6.3 \times 10^{-7}$ . In the warm-hot gas case,

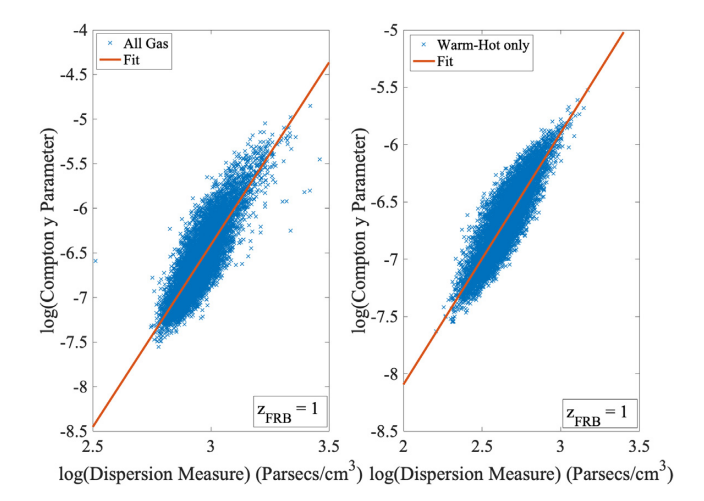


**Figure 6.** Log-log plot of the Compton y parameter from all gas (a) and from only warm-hot gas (b) for FRBs at redshift 1. Each set of data is fit using a linear model. The results are from 10 000 trials.

the mean of the Compton y parameter is  $2.7 \times 10^{-7}$  with a standard deviation of  $2.1 \times 10^{-7}$ .

We should note that equation (7) is not directly observable, since one is not readily able to isolate both y and DM due to warm-hot gas (or WHIM) only. Thus, the discussion is mainly academic and for our own understanding. However, equation (6) is directly observable, and the computed Compton y parameter provides a valuable check on the DM due to the IGM with an independent constraint.

#### 4 CONCLUSIONS

We study the dispersion measures of fast radio bursts due to the intergalactic medium, using cosmological hydrodynamic simulations. Detailed distributions of DM are presented. We quantify the contributions to DM from three phases of gas in the IGM at different temperatures. We find that the hot gas component ( $T > 10^7 \rm K$ ), on average, makes a minor contribution ( $\leq 5$  per cent) to the overall DM. Cold ( $T < 10^5 \rm K$ ) and warm-hot ( $T = 10^5 - 10^7 \rm K$ ) gas components make comparable contributions to DM for FRBs at z = 1, with the (former, latter) component making an increasingly larger contribution towards (higher, lower) redshift.

We calculate the Compton y parameter and find that  $y \propto DM^4$  (equation 6). This correlation provides an additional constraint on the nature of the DM of FRBs, since y may be measurable or at least cross-correlation between observed y and DM may be measurable. Calibrated by the relative contribution of warm-hot gas to the overall DM, the distribution of DM observed will provide a new method to infer the WHIM hence the missing baryons.

#### **ACKNOWLEDGEMENTS**

Computing resources were in part provided by the NASA High-End Computing (HEC) Program through the NASA Advanced Supercomputing (NAS) Division at Ames Research Center. The research is supported in part by NASA grant 80NSSC18K1101.

#### DATA AVAILABILITY

Data is available from the author upon request.

#### REFERENCES

Bertschinger E., 2001, ApJS, 137, 1

Bryan G. L., Norman M. L., 1998, ApJ, 495, 80

Cen R., Chisari N. E., 2011, ApJ, 731, 11

Cen R., Ostriker J. P., 1999, ApJ, 514, 1

Cooksey K. L., Prochaska J. X., Chen H.-W., Mulchaey J. S., Weiner B. J., 2008, ApJ, 676, 262

Danforth C. W., Shull J. M., 2005, ApJ, 624, 555

Danforth C. W., Shull J. M., 2008, ApJ, 679, 194

Danforth C. W., Shull J. M., Rosenberg J. L., Stocke J. T., 2006, ApJ, 640, 716

Danforth C. W., Stocke J. T., Shull J. M., 2010, ApJ, 710, 613

Davé R. et al., 2001, ApJ, 552, 473

Davé R., Hernquist L., Katz N., Weinberg D. H., 1999, ApJ, 511, 521

de Graaff A., Cai Y.-C., Heymans C., Peacock J. A., 2019, A&A, 624, 48

Deng W., Zhang B., 2014, ApJ, 783, L35

Fukugita M., Hogan C. J., Peebles P. J. E., 1998, ApJ, 503, 518

Inoue S., 2004, MNRAS, 348, 999

Ioka K., 2003, ApJ, 598, L79

Keating L. C., Pen U.-L., 2020, MNRAS, 496, L106

Kirkman D., Tytler D., Suzuki N., O'Meara J. M., Lubin D., 2003, ApJS, 149, 1

Komatsu E. et al., 2009, ApJS, 180, 330

Lorimer D. R., Bailes M., McLaughlin M. A., Narkevic D. J., Crawford F., 2007, Science, 318, 777

McQuinn M., 2013, ApJ, 780, L33

Narayanan A. et al., 2011, ApJ, 730, 15

Narayanan A., Wakker B. P., Savage B. D., 2009, ApJ, 703, 74

Nicastro F. et al., 2018, Nature, 558, 406

Niino Y., 2020, preprint (arXiv:2005.12891)

Oegerle W. R. et al., 2000, ApJ, 538, L23

Persic M., Salucci P., 1992, MNRAS, 258, 14P

 $Petroff\ E.\ et\ al.,\ 2016,\ Publ.\ Astron.\ Soc.\ Aust.,\ 33,\ e045$ 

Petroff E., Hessels J. W. T., Lorimer D. R., 2019, A&AR, 27, 4

Prochaska J. X., Chen H.-W., Howk J. C., Weiner B. J., Mulchaey J., 2004, ApJ, 617, 718

Savage B. D., Sembach K. R., Tripp T. M., Richter P., 2002, ApJ, 564, 631

Savage B. D., Lehner N., Wakker B. P., Sembach K. R., Tripp T. M., 2005, ApJ, 626, 776

Savage B. D., Narayanan A., Lehner N., Wakker B. P., 2011a, ApJ, 731, 14

Savage B. D., Lehner N., Narayanan A., 2011b, ApJ, 743, 180

Sembach K. R., Tripp T. M., Savage B. D., Richter P., 2004, ApJS, 155, 351

Tanimura H. et al., 2018, MNRAS, 483, 223

Thom C., Chen H.-W., 2008a, ApJS, 179, 37

Thom C., Chen H.-W., 2008b, ApJ, 683, 22

Thornton D. et al., 2013, Science, 341, 53

Tripp T. M., Savage B. D., 2000, ApJ, 542, 42

Tripp T. M., Savage B. D., Jenkins E. B., 2000, ApJ, 534, L1

Tripp T. M., Sembach K. R., Bowen D. V., Savage B. D., Jenkins E. B., Lehner N., Richter P., 2008, ApJS, 177, 39

Tripp T. M. et al., 2011, Science, 334, 952

This paper has been typeset from a  $T_EX/IAT_EX$  file prepared by the author.